# Improved Detection of the First-Order Region for Direction-Finding HF Radars Using Image Processing Techniques

ANTHONY KIRINCICH

*Woods Hole Oceanographic Institution, Woods Hole, Massachusetts*

(Manuscript received 18 August 2016, in final form 18 January 2017)

ABSTRACT

For direction-finding high-frequency (HF) radar systems, the correct separation of backscattered spectral energy due to Bragg resonant waves from that due to more complex double-scattering represents a critical first step toward attaining accurate estimates of surface currents from the range-dependent radar backscatter. Existing methods to identify this ''first order'' region of the spectra, generally sufficient for lower-frequency radars and low-velocity or low-surface gravity wave conditions, are more likely to fail in higher-frequency systems or locations with more variable current, wave, or noise regimes, leading to elevated velocity errors. An alternative methodology is presented that uses a single and globally relevant smoothing length scale, careful pretreatment of the spectra, and marker-controlled watershed segmentation, an image processing technique, to separate areas of spectral energy due to surface currents from areas of spectral energy due to more complex scattering by the wave field or background noise present. Applied to a number of HF radar datasets with a range of operating frequencies and characteristic issues, the new methodology attains a higher percentage of successful first-order identification, particularly during complex current and wave conditions. As operational radar systems continue to expand to more systematically cover areas of high marine traffic, close approaches to ports and harbors, or offshore energy installations, use of this type of updated methodology will become increasingly important to attain accurate current estimates that serve both research and operational interests.

## 1. Introduction

High-frequency radars are now being used on an operational basis to routinely observe surface currents over the coastal ocean at scales from 20 to 150 km offshore (see Paduan and Washburn 2013 for a review). The compact direction-finding SeaSonde radar system, commercially manufactured by CODAR Ocean Sensors (COS), dominates the number of installed systems worldwide. Thus, much of the operational and scientific uses of radar-derived surface currents rely on the processing algorithms used by COS's operational software, the SeaSonde Radial Suite (COS 2013), to convert the observed backscatter energy into surface currents from known azimuthal directions.

In these systems, the correct identification of the first-order region of the power spectra, where the signal is due to the coherent backscatter from Bragg resonant waves (Barrick 1972; Lipa et al. 2006; Paduan et al. 1999), is a critical step toward attaining accurate estimates of surface currents. The existing method used to determine these limits within the SeaSonde Radial Suite relies on a series of user-defined parameters (COS 2013; Table 1) that are initially set upon installation of a system and infrequently altered thereafter. In general, this methodology leads to sufficiently accurate first order identification for lower frequency (4–6 MHz) systems and locations with weak velocities or small wave regimes. However, application of the existing method to higher-frequency systems (20–50 MHz) as well as locations with strong currents or variable wave regimes can lead to more frequent failures of the method, resulting in elevated velocity errors. Additionally, spectral noise from such factors as intermittent radio frequency (RF) noise, ionospheric returns, or moving offshore structures such as offshore wind energy installations can confound the existing method if not properly tuned for the instantaneous conditions present.

This paper presents an alternative methodology that uses a single, globally relevant smoothing length scale to reduce the number of user-defined parameters and marker-controlled watershed segmentation (Meyer 1994), an image processing technique, to separate areas

*Corresponding author*: Anthony Kirincich, akirincich@whoi.edu

DOI: 10.1175/JTECH-D-16-0162.1

TABLE 1. SeaSonde FOL parameters.

| Parameter | Definition | Usage |
|---|---|---|
| noisefact | Noise threshold | Data below noisefact*(noise floor) are eliminated. |
| nsm | Smoothing length scale | Used to set in spectral points. |
| fdown | First-order factor | Used (as amax[a]/fdown) to set start point of search for null between first- and second-order energy. |
| flim | Low-energy threshold | Used (as amax[a]/flim) to eliminate spectral points that are too far below the peak energy. |
| currmax | Current threshold | Sets the maximum current speed allowed. |
| ionfact | Ionospheric contamination factor | Used to find near Bragg energy greater than ionfact*(Bragg Energy). |

[a] The quantity amax is the range-dependent maximum power.

of spectral energy associated with useable observations of surface currents from wave- or noise-dominated spectral energy. Importantly, it considers the total range-dependent spectra in a holistic approach, what an operator would naturally do "by eye," allowing the method to correctly include complex patterns of Bragg energy into the estimated first-order region. The paper is organized as follows: additional details on the presently used methodology are presented first, followed by details on the proposed methodology, referred to here as the ImageFOL method, and the results of comparative tests on a number of problematic SeaSonde datasets. A MATLAB-based software package that performs the calculations described in the text is being made publicly available (Kirincich 2016a) to facilitate additional testing and further advancements.

## 2. Background

The largest contribution to the returning power (the backscatter) from a transmitted signal in the HF spectrum is the scatter from surface waves whose wavelength is half the wavelength of the radar (Crombie 1955, Fig. 1). These waves are known as the Bragg resonant waves, in analogy to scattering from a crystal or a diffraction grating. In the absence of a surface current, scatter from the Bragg waves produce two peaks in the power spectrum of the radar return at plus/minus the frequency of the Bragg wave (the "first order" region; Barrick 1972). Advection of these waves by a current produces a Doppler shift in the location of the first-order peaks and, hence, the observed displacement in frequency can be used to infer the component of the current along the radar beam. The Bragg peaks are flanked by a weaker "second order" continuum (Barrick and Weber 1977, Fig. 1) due to double scattering from two wave periods, which contains contributions from all ocean wave components longer than the Bragg waves.

For direction-finding systems such as the SeaSonde, identification of the boundaries between the primary or first-order Bragg region and the weaker or second-order continuum within the observed backscatter spectra is one of the first steps toward estimating the radial velocities. Referred to as the first-order limits (FOLs), these boundaries are identified using the self-spectra of the monopole receive antenna (COS 2013), as they alone contain a full response from all azimuthal directions. The SeaSonde Radial Suite, COS's operational software package, relies on a proprietary calculation, performed separately on the self-spectra of each range bin, to estimate the FOLs. The calculation uses a set of five user-defined parameters (COS 2013; Table 1) that act to compare the power of the spectra near each of the Bragg lines to the power of the areas adjacent to it, in order to identify significant local minima in power, which are assumed to be the gap in spectral space between the first-order region and the flanking second-order regions. A number of the parameters (Table 1) are used to limit the result to spectral areas some level above the noise floor, or with corresponding current speeds less than some value. All spectral points (in range and Doppler frequency) within the designated first-order region are processed using the multiple signal classification (MUSIC) algorithm (Lipa et al. 2006; Schmidt 1986) to define the radial velocities observed by the direction-finding radar system.

It should be noted that phased-array HF radar systems, which use beam forming to isolate each azimuthal direction, also need to identify the first-order region from the second-order continuum, particularly for inverting the observed spectra to estimate the surface gravity wave field. However, as the first-order region is narrower by definition for phased-array spectra after beam forming, defining the first-order limits within phased-array radar results is more straightforward than for direction-finding radar results.

Operationally, the COS FOL parameters are set upon installation of a new SeaSonde system, and are adjusted by trial and error to minimize errors perceived by visual inspection of a few of the initial spectra (COS 2013; Cook et al. 2008). Most parameters (Table 1) are not altered thereafter. Some have only a minor effect on FOL

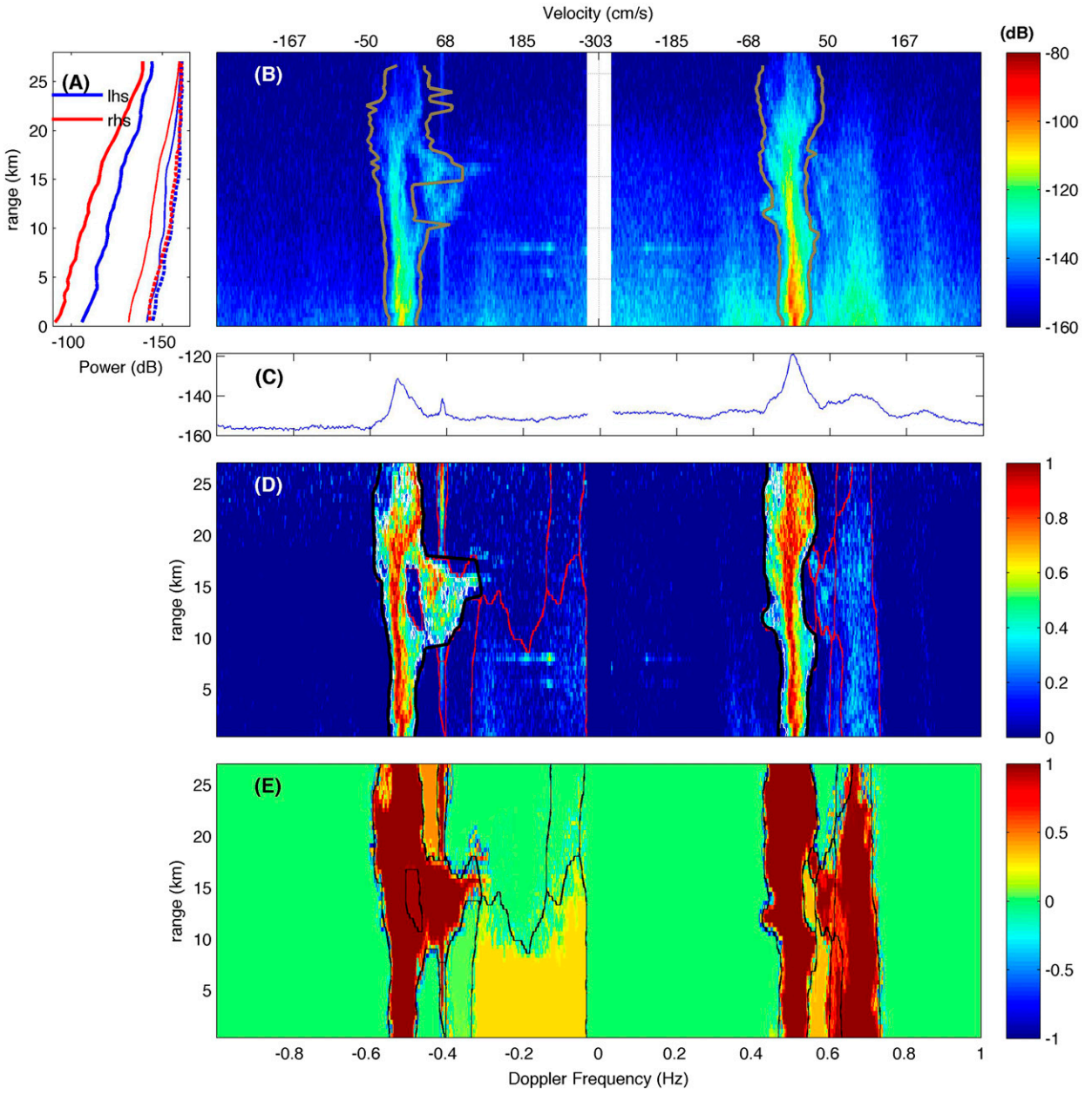


FIG. 1. Important aspects of the ImageFOL method, shown using the ensemble-averaged spectra (i.e., from the *.cs4 file) captured by the monopole of LPWR at 0645 UTC 8 Feb 2011. (a) Range-dependent maximum power (bold solid) mean power (solid), and noise level (dashed) for the lhs (blue) and rhs (right) of the spectra. (b) Spectral power for all ranges and Doppler frequencies (or velocities; color shading) with the first-order line calculations based on well-tuned SeaSonde parameters (gray). (c) Range-averaged power for each Doppler frequency. (d) Preprocessed spectra power in arbitrary units. Estimated watershed "segments" (outlined in red) with those segments overlapping the Bragg region (outlined in black). (e) Processed power in arbitrary units after application of the length-scale-based smoothing and reconstruction, used to compute the MCWS, and estimated watershed segments (outlined in black).

identification (i.e., nsm), while others (fdown, flim) have overlapping effects that may confuse efforts to tune the identification process. For many systems, particularly those operating at lower frequencies (4–5 MHz), this initial tuning of the FOL methods is sufficient and results in few errors in the processing of the data. However, for higher-frequency systems (24–26 and 40–45 MHz), as well as those operating in high and/or variable current environments or variable wave conditions (e.g., near bathymetric shoals, strong currents, or high-wave climates), use of the COS parameters have increased potential either to place second-order wave energy within the first-order limits or

TABLE 2. Test datasets and results.

| Site | LPWR | NWTP | HATY | CORE | STV1 |
|---|---|---|---|---|---|
| Region | Martha's Vineyard | Nantucket | Cape Hatteras | | Oregon |
| Location (lat°, lon;°) | 41.3484, −70.6402 | 41.2420, −70.1070 | 35.2573, −75.5200 | 34.7601, −76.4114 | 46.1764, −123.9784 |
| Center frequency (MHz) | 25.500 | 13.520 | 4.575 | 4.537 | 13.512 |
| Spectral length (points) | 1024 | 1024 | 1024 | 1024 | 512 |
| v_incr ($m\,s^{-1}$) | 0.0115 | 0.0217 | 0.0318 | 0.0321 | 0.0431 |
| Data source | —[a] | —[a] | H. Seim (University of North Carolina) | | M. Kosro (Oregon State University) |
| Complicating issues | Strong tides, Variable waves | Noise | Gulf Stream, Noise | | Strong tides, Swell |
| | | | Image FOL parameters | | |
| vel_scale ($cm\,s^{-1}$) | 20 | 20 | 40 | 40 | 70 |
| Max_vel ($cm\,s^{-1}$) | 200 | 200 | 300 | 300 | 200 |
| SNR_min | 5 | 5 | 5 | 5 | 5 |
| | | | Results | | |
| No. files examined | 2684 | 709 | 278 | 280 | 158 |
| | | | No. of failures by method | | |
| COS FOL | 544 | 161 | 108 | 79 | |
| ImageFOL | 261 | 7 | 17 | 6 | 29 |
| Both | 130 | 14 | 8 | 9 | |
| | | | Failures by method (%) | | |
| COS FOL | 25 | 25 | 42 | 31 | |
| ImageFOL | 15 | 3 | 9 | 5 | 18 |
| | | | Length-scale variability | | |
| $N$ = vel_scale/(100v_incr) | 16 | 8 | 12 | 12 | 16 |
| lhs: dn ± std(dn) | 8.5 ± 3.1 | 5.0 ± 2.0 | 8.6 ± 2.6 | 8.5 ± 2.0 | 8.2 ± 2.7 |
| rhs: dn ± std(dn) | 7.2 ± 2.5 | 5.9 ± 1.9 | 8.8 ± 2.6 | 8.4 ± 2.1 | 6.4 ± 2.0 |

[a] Operated by the author.

to systematically exclude valid first-order energy (i.e., from a consistent phase of the tide) from the identified first-order region. Either type of error can lead to potentially substantial errors in the estimated surface currents.

A sample spectra from a 25-MHz radar site located on Martha's Vineyard, Massachusetts (site LPWR; Table 2), illustrates the potential issues in more complex observations of the spectra (Fig. 1b). For a number of range bins on the left-hand side of the spectra, the first-order region is wide in spectral space with potentially multiple high energy peaks separated by areas that approach background levels. In contrast, the right-hand side of the spectra has much higher energy in the second-order region and a more narrowly defined first-order region. Additional examples of spectra from LPWR (Fig. 2) illustrate both the potential temporal variability of the spectral returns seen at an individual site as well as the flexibility required, both in time and range, to assessing the first-order limits properly.

To be clear, it is certainly possible to tune existing FOL methods in order to achieve reasonable results for an individual spectrum. However, two points should be readily apparent from Figs. 1b and 2: 1) Stronger spatially and temporally variable currents combined with moderate variable wave conditions are transient effects that can be difficult to correctly separate on a consistent basis using a static set of parameters within existing methods. 2) Even within a single realization (i.e., Fig. 1b), a parameter set that gives reasonable results on one-half of the spectra might perform poorly on the other half, due to the large changes in the second-order energy level, as well as the variable spectral location of the second-order energy caused by variable wave conditions. Finally, within the SeaSonde Radial Processing Suite, elevated levels of background noise are identified by a separate parameter (ionfact; Table 1) outside of the COS FOL method and not recorded within the spectral data file.

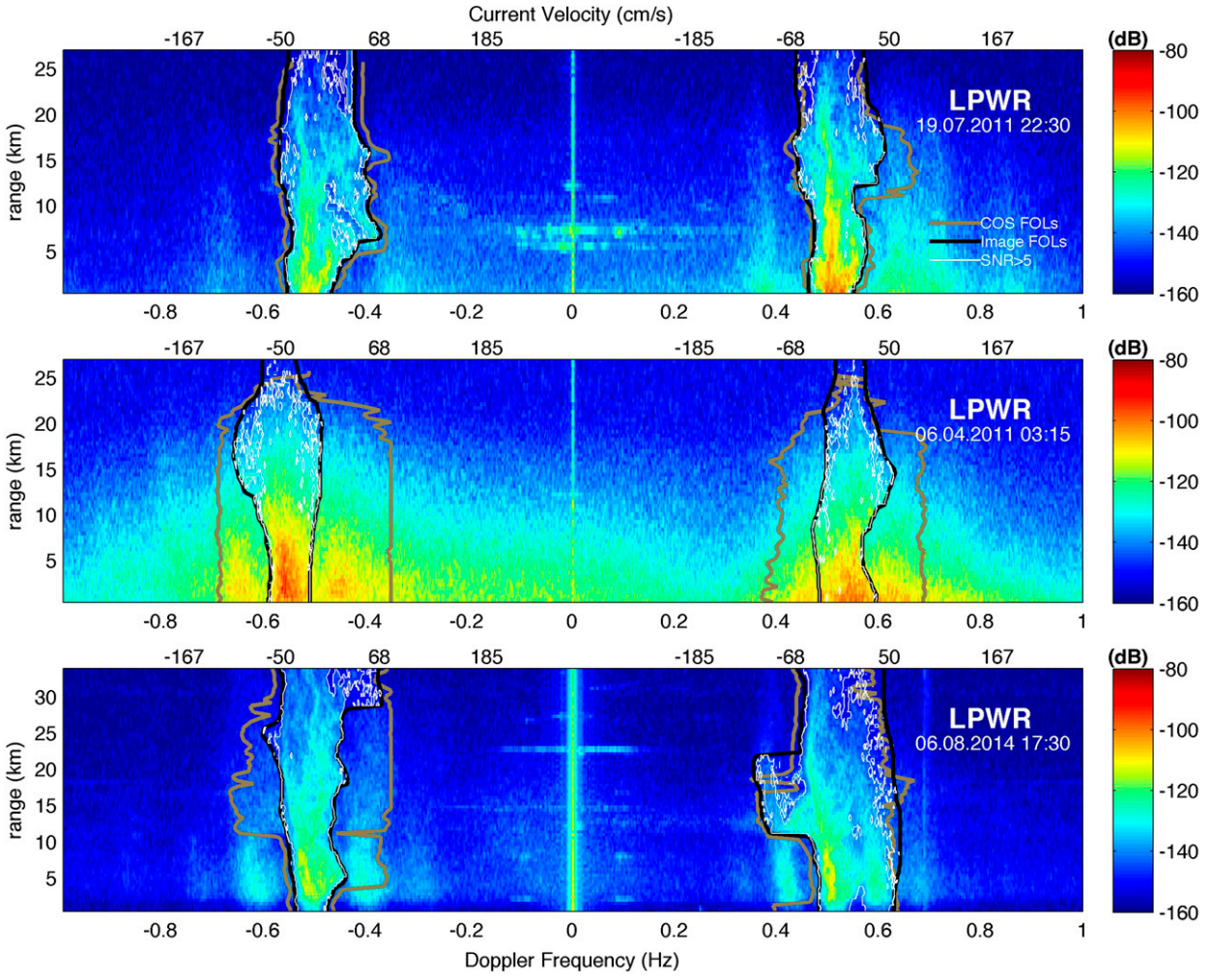


FIG. 2. Sample monopole spectral power for LPWR (color shading), illustrating the potential variability of first- and second-order spectral energies as well as the performance of first-order line calculations based on well-tuned SeaSonde parameters (COS FOLs, gray) and the ImageFOL results (black): (top) 2230 UTC 19 Jul 2011, (middle) 0315 UTC 6 Apr 2011, and (bottom) 1730 UTC 6 Aug 2014. Spectral points within the ImageFOL area that would be passed to the direction-finding algorithm, defined as SNR $>$ 5 above the demeaned, detrended spectra used to estimate the ImageFOLs (see text for details), are shown within the white contour.

## 3. The ImageFOL method

This paper describes a new methodology for delineating the first-order region in direction-finding HF radar spectra that is both more flexible than the present method and requires less tunable parameters. In almost all of the situations described above, or those additionally shown in Fig. 3, an operator with a minimal amount of experience in radar processing can, by visual examination of the spectra, separate the first- and second-order regions. Thus, since our eye can ''see'' where the line should be drawn, a logical step forward is to incorporate image processing techniques to isolate all of the first-order area in a coherent manner.

It will be shown below that image-based FOLs can do as good as current methods for more simply defined spectra, as well as allow for transient high-wave or strong current effects to be captured more consistently in more complex spectra. Additionally, the method requires only three parameters to be set, or ''tuned,'' by the user (Table 2). Similar to existing methods used by COS software, two thresholding parameters are used: a minimum signal-to-noise ratio for viable spectral estimates of the surface currents and a maximum velocity that will be encountered by the radar. The third parameter—a smoothing length scale described in detail below—is critical to the proper delineation of the FOLs.

### *a. Methodological background*

The field of image processing is well developed and numerous techniques exist to examine images and find an object—say, a piece of fruit or a person—and separate it

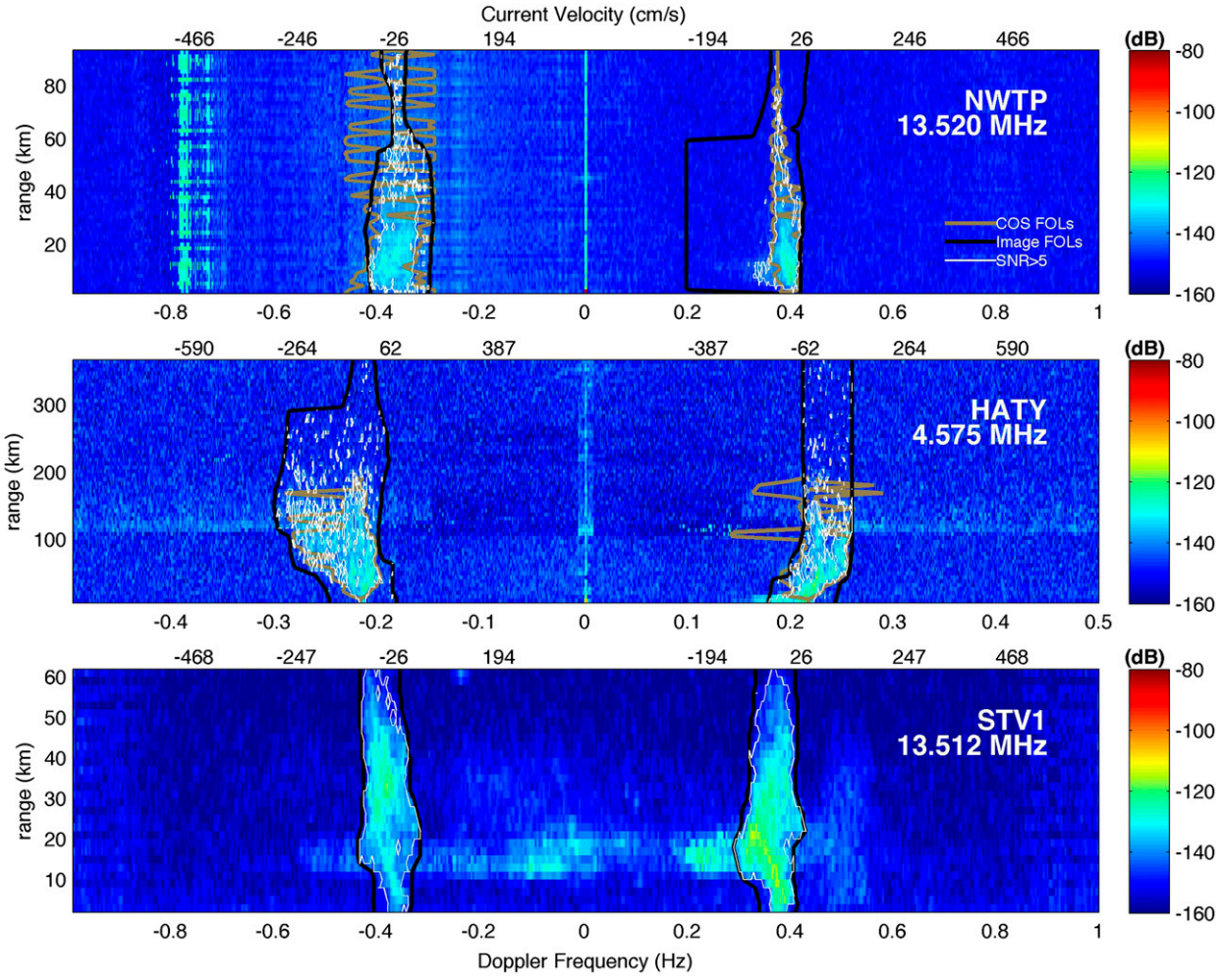


FIG. 3. Sample monopole spectral power (color shading) for sites (top) NWTP, (middle) HATY, and (bottom) STV1. In the two top panels, the calculated first-order lines based on well-tuned SeaSonde parameters (COS FOLs, gray) and the ImageFOL results (black) are shown along with the spectral points within the imageFOL area that would be passed to the direction-finding algorithm, defined as SNR $> 5$ above the de-meaned, de-trended spectra used to estimate the imageFOLs (white contour).

from the rest of the image. The facial recognition algorithms embedded in the photo editing software on a typical personal computer is one example of the field's maturity. The application of these techniques to the problem of correctly determining the first-order region is useful, as this process is effectively the same as what an operator would naturally do by eye. Further, such a method considers the total spectra present in a holistic approach, in contrast to acting on each range bin independently.

The component of image processing of interest here involves image segmentation, or isolating important elements of an image from the background and each other. Numerous algorithms exist in the literature to perform segmentation, including clustering methods, histogram-based methods, edge detection, model-based segmentation, watershed segmentation, and neural networks segmentations (see Shapiro and Stockman 2001 for a full summary). However, because of the natural roll off of spectral power both in range and Doppler velocity that exists within the first-order region, the most viable methodology of interest is watershed segmentation. Watershed segmentation and the watershed transform (Meyer 1994) consider a grayscale image as representing a topographic relief map, where light pixels are high and dark pixels are low, and find individual "catchment basins" that are separated by ridge lines to define watersheds. This segmentation into watersheds is more effective if the basic location of foreground objects are already identified, or marked, relative to the background, and small blemishes have been removed (Mathworks 2013). Thus, a hybrid approach called marker-controlled watershed segmentation (MCWS) is used here.

MCWS couples morphological filtering of the image as pretreatment in order to guide identification of the core areas of objects before using watershed segmentation to determine their boundaries. The image is filtered using a smoothing disk of variable size to highlight areas of minimal change either in the objects or the background. Lighter areas of minimal change that are greater than a threshold area in size are marked as objects, and the watershed transform is applied to find the boundaries around adjacent objects. Thus, the size of the smoothing disk is a critical parameter for proper use of the technique. The MCWS technique is straightforward, well documented (Beucher 1993; Meyer 1994; Gonzalez and Woods 2008), and well cited for use in similar types of tasks within the medical image processing literature (e.g., Pham et al. 2000; Yang et al. 2006). MCWS has recently been adapted for oceanic research applications (Al-Lashi et al. 2016) and is fully integrated into common analysis software packages such as MATLAB, used here for development.

While MCWS is preferred for use here for both performance and convenience, tests between MCWS and other image segmentation techniques, such as edge detection, found that the particular method of segmentation did not matter as much as the preprocessing of the spectra and a keen choice of the smoothing length scale, both of which are described in detail below. Thus, detailed sensitivity tests between image segmentation techniques themselves are beyond the scope of this work.

### b. *Application to HF radar: The ImageFOL method*

In the context of identifying the first-order region using MCWS, the spectral power observed by the monopole (antenna 3) is considered here to be the image and the Bragg region, the continuous region of elevated spectral power due to Bragg scattering, is the object we seek to isolate. However, small-scale (in power and spectral space) variations, analogous to blemishes on a photo, on or near the Bragg region exist within the spectra. A user-defined length scale sets the size of the smoothing disk, which is used both to smooth out small variations to guide object identification and the watershed transform and to set the minimum size of an object. Additionally, the ImageFOL method uses a number of pretreatment steps based on important properties of the first- and second-order regions of HF radar backscatter and how they are represented in a typical spectra—that is, what operators generally develop a feel for over time—to further constrain the MCWS calculation. These steps both prepare the image for the MCWS and are used to adjust the user-defined length scale based on the oceanic conditions observed within the spectra.

Somewhat independent of FOL identification, RF noise can occur for various reasons, within random spectral areas (range, Doppler velocity dependence, and energy level), and must be accounted for. Broadband energy that simply raises the noise floor at all or a given range bin can be well constrained and eliminated by the ideas described below. Isolated points, or more importantly areas/lines of noise energy at narrow bands of Doppler frequency, are also easily ignored by the present methodology except when they overlap the Bragg region itself. However, if significant RF noise exists within the Bragg region, then it becomes difficult to tell whether an observation is signal or noise based on the spectral patterns available during FOL estimation. While other methods within an HF radar processing stream outside of the FOL estimation component, such as a postprocessing analysis of the azimuthal distribution of radial velocity, could be used to identify noise versus signal on a finer scale within the Bragg region, these are beyond the scope of the present work. Thus, we seek to identify such events so that the entire Bragg region in the given spectral half can be ignored from the radial velocity analysis, preventing potentially erroneous data from being considered further.

### c. *Implementation*

- **Required inputs:** In addition to the spectral power observed by the monopole and basic information about the radar itself (operating frequency, velocity resolution, etc.), three user-defined parameters are used within ImageFOL: The first parameter, max_vel, the absolute maximum current speed encountered, and the second parameter, snr_min, the minimum power above the range-dependent mean power allowed, are similar to those used by the COS FOL method. The third, vel_scale, represents a velocity scale (e.g., 20 $\mathrm{cm\,s^{-1}}$) that is used to set $N$, the core smoothing length scale used throughout ImageFOL, as $N$ = vel_scale/(100v_incr), where v_incr is the Doppler velocity resolution of the spectral file. Defining $N$ based on vel_scale allows the method to account for the effects of the velocity resolution of the spectra, a function of the spectral length and radar frequency in a user-friendly way. The parameter vel_scale can be defined either visually—for example, one-half of the spectral width of most of the Bragg energy—or mathematically—for example, the temporal standard deviation of the observed velocities—and adjusted from there to suit the user's needs.
- **Pretreatment:** Using $N$ as a smoothing length scale, spectra are filtered in range to calculate the mean energy separately for each spectral half (Fig. 1a), corresponding to the Bragg returns from incoming

[right-hand side (rhs)] and outgoing [left-hand side (lhs)] Bragg waves. This range-dependent mean profile is subtracted from each half to form the spectral anomaly. Values less than zero are replaced with zeros. All actions are performed separately on the left and right halves of the spectra, as the characteristics of the first, second, and background energies present due to incoming (lhs) and outgoing (rhs) waves can be markedly different. Using the mean spectral energy was found to be a more reliable way to determine a lower bound for the FOL calculation than using the noise floor times some user-defined value. Given equal first-order energy, increased wave activity would increase the second-order energy present, which would result in a higher mean energy and thus an increased lower bound. The spectral anomalies are then normalized by the range-dependent maximum power (Fig. 1a) to transform the anomaly into a gradient function spanning 0–1 at each range (Fig. 1d). This acts to sharpen the difference between Bragg and non-Bragg energy at higher range bins and normalize for the roll off of Bragg energy with range.

- **Adjusting the length scale:** The length scale $N$ is used to set the initial size of the smoothing disk used by MCWS. However, the size of the disk is adjusted to account for both the magnitude and location of the second-order energy present. This is a critical aspect of the methodology, allowing the MCWS to be flexible to a wide range of noise and signal conditions. Stronger wave/wind conditions should use a smaller disk, while no wave, strong current conditions should use a wider disk. Strong swell conditions, which push the second-order energy closer to the Bragg region, require a smaller disk, somewhat independently of the relative strength of the second-order energy. ImageFOLs account for these effects by decreasing the initial length scale and thus the size of the MCWS smoothing disk by a noise factor, defined as the difference between the mean second-order energy and the noise floor. This noise factor is doubled if the distance between the inner edges of the second-order regions that flank the Bragg region is smaller than $3N$, typical of strong swell conditions. The inner edges of the second-order regions are defined to be the first local minimum to the left and right of the Bragg peaks of the range-averaged spectra (Fig. 1c). A factor of $3N$ is used here due to the space, in spectral points, needed to define the basins between adjacent ridges within the MCWS. The altered length scale, defined here as dn, is always less than $N$, different for each spectral half, and highly variable in time (Table 2).
- **Screening for RF noise contamination:** As described above, elevated RF noise that contributes to higher background noise levels (i.e., noise exists at all ranges and Doppler velocities) and RF noise that is isolated to individual range bins (i.e., horizontal lines in the spectra) can be accounted for via pretreatment. Elevated RF noise that exists at isolated Doppler frequencies can be separated from the Bragg energy using MCWS except when the noise overlaps with the Bragg frequencies. Generally, high levels of Doppler frequency–dependent RF noise at or near Bragg Doppler frequencies have energy levels that are somewhat independent of range, while in contrast typical first-order energy decreases to lower power at higher ranges. Thus, a viable test for whether noise is a dominant part of the signal at near-Bragg frequencies is whether the range-dependent energy level at Bragg$\pm N$ frequencies for each spectral half rolls off at similar levels. If the ratio between the roll off on a spectral half to the roll off on the other spectral half is less than 0.4–0.5 (defined as an internal constant based on inspection of the datasets described below), then no FOLs are returned for the spectral half, effectively removing it from radial processing.
- **MCWS application:** MCWS acts to first saturate the top 100 − 2dn percentile of the altered image (Fig. 1e) to create a plateau effect within the Bragg region, allowing markers to be placed at these regions of minimal change before applying the watershed transform. MCWS is applied iteratively, decreasing dn until a minimum number of four segments are found within each spectral half. This ensures that segments are identified at the Bragg region and on either side of the Bragg region. Applied to the test datasets below, multiple iterations were rarely needed.
- **Postprocessing:** The MCWS procedure may generate multiple segments that incorporate the first-order region. Here again, dn is used to define those segments that have area within ±dn from the Bragg line as part of the first-order region. Of these segments, all points within them that have radial velocities less than max_vel and pretreatment energies greater than snr_min are assumed to be first-order energy (Fig. 1d, white contour).

## 4. Application

### *a. Test datasets*

Spectral results from five different HF radar installations (Table 2), including one 25-MHz system (LPWR; Figs. 1 and 2), two 4-MHz systems (HATY and CORE; Fig. 3) and two 13-MHz systems (NWTP and STV1; Fig. 3) are used as test datasets to validate the performance of the ImageFOL method. The data

TABLE 3. LPWR results against near-surface ADCP-based velocities.

| Bottom | Range | Angle from | Raw 15-min samples | | | | Half-hourly averages | | | |
|---|---|---|---|---|---|---|---|---|---|---|
| | | | COS FOLs | | ImageFOLs | | COS FOLs | | ImageFOLs | |
| Lander[a] | (km) | Boresight (°)[b] | $R$ | RMSD (cm s$^{-1}$) | $R$ | RMSD (cm s$^{-1}$) | $R$ | RMSD (cm s$^{-1}$) | $R$ | RMSD (cm s$^{-1}$) |
| B | 8.8 | 35 | 0.75 | 10.1 | 0.75 | 10.0 | 0.79 | 9.0 | 0.80 | 8.6 |
| C | 2.5 | −42 | 0.77 | 9.1 | 0.77 | 9.0 | 0.84 | 7.4 | 0.86 | 6.8 |
| D | 8.5 | −32 | 0.70 | 10.5 | 0.72 | 10.0 | 0.77 | 8.8 | 0.77 | 8.7 |
| F | 12.5 | −48 | 0.62 | 14.1 | 0.68 | 13.5 | 0.64 | 13.3 | 0.66 | 12.7 |
| G | 7.1 | −78 | 0.93 | 11.5 | 0.93 | 10.8 | 0.94 | 11.0 | 0.94 | 10.3 |
| I | 7.8 | −48 | 0.79 | 10.8 | 0.81 | 10.1 | 0.82 | 9.7 | 0.83 | 9.3 |

[a] Bottom lander locations shown in Fig. 4.
[b] As estimated, negative angles from boresight—that is, directly offshore—indicates locations to the east of the radar site.

products used here (the *.cs4 or *.cs files as defined by the SeaSonde Radial Suite; COS 2013) represent the ensemble averaged spectra used to estimate the initial radial velocities (referred to as the ''radial shorts''; COS 2013) that are subsequently time averaged over a larger 30–180 min time window into the radial velocity product normally reported by SeaSonde systems. Each dataset was chosen due to the occurrence of complicating issues that prevent existing methods from achieving consistent and correct identification of the first-order region (Figs. 2 and 3). Both 4-MHz systems (HATY and CORE) observe portions of the Gulf Stream where radial currents reach upward of 3 m s$^{-1}$, waves are highly variable, and significant background noise issues exist (H. Seim and S. Haines 2016, personal communication). The STV1 data contain strong tidal currents associated with the Columbia River plume as well as narrow-banded high-energy swell (M. Kosro 2016, personal communication). The 13-MHz NWTP data have an issue with frequent intermittent RF noise existing at variable Doppler frequencies. And finally, the 25-MHz LPWR data used for much of the ImageFOL testing exist in a low RF noise environment but have highly variable currents and waves that produce complex patterns within the spectra (Figs. 1 and 2).

### b. *Assessment strategy*

Two types of tests were performed to assess the performance of the ImageFOL method in finding the first-order region in comparison to existing methods. First, visual inspection of the estimated first-order limits for all available spectral results (Table 2) was performed to assess how well either the COS FOL method or the ImageFOL method was able to correctly separate the first-order region from the second-order or noise energies. Failure was defined as incorrect estimates of the first-order region for greater than three range bins of a given ensemble-averaged spectra.

Second, the results from LPWR for both the COS and ImageFOL methods were used to quantify the potential for error reduction using comparisons to the surface-most velocity observations of six bottom-mounted upward-looking acoustic Doppler current profilers (ADCPs) deployed within the radar's range during August 2014. Described in detail by de Paolo et al. (2015) and Kirincich and Lentz (2017), locations of the ADCP results used here were 2.5–12.5 km away from the radar in water depths of 12–25 m (Table 3; Fig. 4) This test used each realization of the ensemble-averaged spectra (a 15-min average of multiple spectral estimates) and the FOLs from both methods to estimate radial velocities (i.e., radial shorts; COS 2013) following Lipa et al. (2006) and Kirincich (2016b). For the nearest radar range–azimuthal bin to each ADCP location, the raw time series of radial velocities, with no subsequent quality assurance–quality control (QA–QC) techniques applied, were compared to the component of the horizontal velocity vector from the surface-most ADCP depth bin, generally 2–4 m below the surface, aligned with the bearing between the radar and ADCP locations. The along-radial ADCP velocities were augmented with an estimate of the Stokes drift based on nearby wave observations to account for this key difference between the two observation techniques (see Kirincich et al. 2012 for details).

Comparisons between the radial velocities observed by LPWR during August 2014, processed using both FOL methods, and the near-surface velocities observed by ADCPs were assessed by estimating the cross correlation at zero time lag and the rms difference (RMSD) between the radar and ADCP radial velocity time series for the raw 15-min estimates of the radial velocities (Table 3). In general, a large number of physical and instrumental factors can lead to differences between ADCP and radar observations. Published estimates of rms difference range from 5 to 20 cm s$^{-1}$ (see Paduan and Washburn 2013) with 5–6 cm s$^{-1}$ representing a likely lower bound for well-sampled time-averaged radar results in less complex

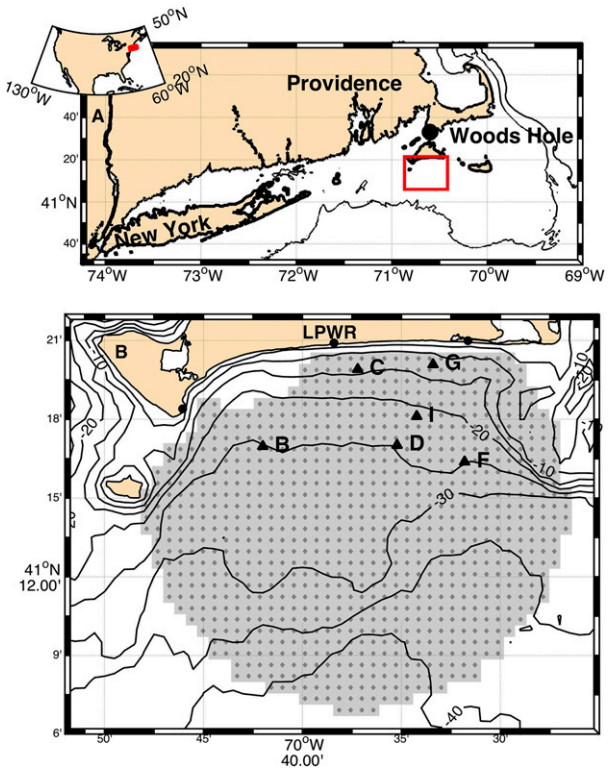


FIG. 4. (a) The southern New England Shelf, denoted in red relative to North America (inset top left), and the study area south of Martha's Vineyard (red box). (b) Coverage map for the WHOI HF radar system with the locations of the radars (dots) and the (triangles) used in the analysis. LPWR is the center of the three radars that contribute to the coverage area.

current environments. Thus, rms differences greater than these lower bounds represent errors or differences due to additional instrumentation or methodological issues that could be reduced via additional processing methods (see discussion below). Comparisons also are given for half-hourly averaged radial velocities to determine the potential importance of the FOL method on more commonly used data products (Table 3).

### c. *Results*

For the COS FOL method, FOL results (the Alim output; COS 2013) were taken from the resource fork of the data file itself and not calculated in this study. For each of the datasets used, the existing COS FOLs represented the best "well tuned" state of the operational HF radar system possible using the COS parameters and methodology. For the ImageFOL method, only two of the three input parameters were varied among the test datasets used here (Table 2). A higher max_vel was used for HATY and CORE to account for the strong Gulf Stream velocities present in those results. The characteristic velocity scale, vel_scale, was set at 20 cm s$^{-1}$ for LPWR and NTWP and at 40 cm s$^{-1}$ for HATY and CORE, a-priori based on the width of the Bragg region in Doppler frequency. For STV1, vel_scale was set at a larger value of 70 cm s$^{-1}$ after viewing one-third of the files used here, due to the tidal phase dependence of the characteristic issue.

The first test aimed to determine, by inspection, whether the ImageFOL methodology was able to more accurately determine where the lines separating the first- and second-order regions should be drawn. While failure was defined as bad FOLs at greater than three range bins in a given file, compared to the assessment of a trained operator, it should be noted that both methods were generally successful at greater than one-half of the range bins in all of the files examined. Reported here in terms of the percent of files with failures due to the large difference in the number of data files observed (Table 2), failures of the COS FOL method occurred in 25%–40% of files for those sites with COS FOL results. ImageFOL failure rates were lower, at 3%–18%, with failures at sites LPWR and STV1 being the largest. At LPWR, while the ImageFOL results are more often able to successfully delineate the first-order region in complex current and high-wave environments (e.g., Fig. 2, top panels), the method still fails during complex currents and narrow-banded low-frequency swell (e.g., Fig. 2, bottom panel). At STV1, failures of the ImageFOL method were primarily driven by exclusion of strong surface currents in a narrow range to the left of the rhs Bragg region, which become partially separated from the main Bragg peak over the course of a tidal cycle (Fig. 3). In contrast, NWTP and both 4-MHz sites have large improvements in first-order line identification, mostly due to the noise removal threshold for NWTP but range-dependent complex velocities for the 4-MHz sites (Fig. 3).

In the second test, comparisons between the radial velocities observed by LPWR during August 2014, processed using both FOL methods, and the near-surface velocities observed by in situ ADCPs (Table 3) showed improved comparisons between the radar and the ADCP due to the FOL method alone, which suggests that the method with a lower rms difference has reduced errors relative to the other. For comparisons using the raw 15-min radial velocities, the ImageFOL rms difference results were consistently less than the COS FOL rms differences. West of the radar or close to the coast (landers B and C in Table 3), the reductions were generally small [$O(0.1)$ cm s$^{-1}$]. In contrast, locations to the east of the radar, at negative bearing angles from boresight, had larger [$O(0.5–0.7)$ cm s$^{-1}$] reductions in rms differences. Correlation coefficients

were generally the same or higher for ImageFOL results. These trends persist for comparisons using the more typical 30-min averaged radial velocities, with the ImageFOL rms difference being an average of 0.5 cm $s^{-1}$ less than the COS FOL rms differences. Previous studies of the coastal ocean offshore of Martha's Vineyard (Wilkin 2006; Kirincich et al. 2013; Kirincich 2016c) have shown that amplitudes of the surface tidal velocities are strong and spatially variable to the east of LPWR, where landers F, G, and I were located. Thus, the west-to-east increase in the difference between COS FOL and ImageFOL results is consistent with the broader trend of more complex radial velocities present to the east.

## 5. Discussion

Both of the assessment tests employed here suggest that the ImageFOL methodology outperforms standard methods with little tuning for the individual type of spectra or site characteristics. While a number of the scaling and pretreatment factors used in ImageFOL have parallels to that employed by the COS method, a key methodological difference is the holistic approach ImageFOL makes to consider all range bins at once. Indeed, much of the gains in successful FOL identification come from the inclusion of areas of spectral energy that are ''detached'' from the range bin peak but ''attached'' to high-energy areas at adjacent range bins. Additionally, COS methods tended to include waves when the second-order energy was high and/or broad banded in Doppler frequency, suggesting that the COS parameters are simply not flexible enough to adapt to the potential range of variability present (e.g., Fig. 2). In contrast, the ImageFOL method essentially has one tunable parameter, vel_scale, making refinement for a new radar configuration more straightforward.

The largest fraction of identification errors using the ImageFOL method occurs during strong currents and narrow-banded, long-period swell. This represents the most difficult non-noise conditions for either method to successfully identify without changing parameters so much that other failure modes become more important. For example, at SVT1 near the Columbia River, using vel_scale = 40 cm $s^{-1}$ resulted in 37 failures, all due to first-order energy falling outside of the FOLs. Increasing to vel_scale = 70 cm $s^{-1}$ gives fewer failures, 29 in total, but 4 are now due to second-order energy being included within the FOLs. Further increases in vel_scale result in further increases in the number of failures, with most of the failures coming from second-order energy being included in the FOLs. Additionally, in-depth analysis of failures during swell conditions such as that seen in Fig. 2 suggests that a poor identification of the inner edge of the second-order region within the range-averaged spectra (i.e., Fig. 1c) can lead to an elevated dn, contributing to failures. While this provides a pathway for further improvement of the method, these swell-dominated areas are generally weaker in power than the true Bragg region. Thus, coupling the ImageFOL method with a data quality processing step that performs power-weighted averaging of the radial velocity results (Kirincich et al. 2012; de Paolo et al. 2015) might act to minimize the potential errors due to these methodological failures.

The ImageFOL method is also adept at detecting noise occurring in or adjacent to the Bragg region. It is not known how many of the failures of the COS FOL method found at NWTP would have been captured by the ionospheric interference check used by the SeaSonde Radial Processing Suite or passed through to the radial velocity calculation. Additionally, the COS check compares the energy within the identified FOL to that immediately outside of it, using the threshold value to determine whether to ignore the Bragg region at the given range bin (COS 2013). For narrow-banded in Doppler frequency, noise occurring within the Bragg region, the Bragg region itself is contaminated but potentially not identified following this approach.

The LPWR radial velocity comparisons to in situ ADCP velocities quantified the amount of error reduction possible solely due to refined FOLs. Considering the raw 15-min radial velocity results, reductions in rms difference were largest in locations with stronger, more variable currents and times of stronger waves. Averaging to one-half-hour increments led to rms differences that were 1–3 cm $s^{-1}$ lower than that found for the raw 15-min radial velocities (Table 3) but that still contained notable reductions in rms differences for the ImageFOL method compared to COS FOLs. While the total reductions in rms difference were small relative to the absolute rms differences (i.e., 5%–10%, Table 3), they still represent a potentially significant part of the increase in rms difference, or error, above the lower error bound of 5–6 cm $s^{-1}$ observed for HF radars (Paduan and Washburn 2013). In terms of this lower bound, previous works have found that the direction-finding algorithm itself contributes 3–4 cm $s^{-1}$ of error (Laws et al. 2010) and the near-surface shear between the radar at the surface and the ADCP below can account for 2–3 cm $s^{-1}$ of rms difference (Graber et al. 1997). The error reduction seen here, which exists in addition to these and other sources of rms difference or error, should be

considered to be one aspect of the total error budget for radial velocities. Thus, it is most useful to consider the effectiveness of the method in reducing the magnitude of the errors observed above the 5–6 cm $s^{-1}$ lower bound. In this context, the 0.5 cm $s^{-1}$ mean error reduction simply due to the improved the FOL method can reduce the amount of error above the lower bound by up to a third at some sites (Table 3). Additional QA–QC steps such as spatial smoothing, despiking the radial velocity time series via standard methods (Halle 2008; NDBC 2009), or more advanced non-velocity metric-based QA–QC steps (Kirincich et al. 2012) have been shown to yield reductions that account for significant portions of the remaining error budget.

While the test datasets were chosen specifically for the difficult conditions for FOL identification present, both methods still have nonzero failures and, thus, more work is needed to understand how the remaining failures—particularly in large-current and high-swell environments—can be addressed in a systematic way. For this reason, and to spur additional development of HF radar signal processing in a coherent way, a ''developer'' kit for the ImageFOL method is available publicly online (Kirincich 2016a). New FOL methods such as this could be incorporated into an operator's processing stream in two ways: either 1) via the user-defined scripts section of the existing SeaSonde Data Processing Suite (COS 2013) or 2) within an offline or parallel processing stream that incorporates the methodology made available here into the HFR_Progs MATLAB toolbox to load and analyze SeaSonde-type HF radar datasets. The data sent by the WHOI-owned HF radar systems to the NOAA/Integrated Ocean Observing System (IOOS)-sponsored national network of HF radars already incorporates these and other advanced methods (Kirincich et al. 2012; de Paolo et al. 2015; Kirincich and Lentz 2017) into the real-time operational data processing.

## 6. Conclusions

An alternative methodology for first-order region identification is presented that uses a single and globally relevant smoothing length scale, careful pretreatment of the spectra, and marker-controlled watershed segmentation to separate areas of spectral energy due to surface currents from areas of spectral energy due to more complex scattering as a result of the wave field or background noise present. Applied to a number of HF radar datasets with a range of operating frequencies and characteristic issues, the ImageFOL method attains a higher percentage of successful first-order limit identification, particularly during complex current and wave conditions. In comparison, existing identification methods more frequently fail in higher-frequency systems and/or locations with more variable current, wave, or noise regimes, leading to elevated radial velocity errors. Carried through the remainder of the HF radar processing methods to vector surface currents, these errors can lead to increased noise levels in the surface current estimates and potential biases in the time-averaged surface currents.

While existing methods are likely to be sufficient for HF radar installations in low-current and low-wave-energy environments, future expansions of operational HF radars are likely to focus on higher-frequency systems to more systematically cover areas of high marine traffic and close approaches to ports and harbors, all of which entail complex current environments, such as flow around headlands, reefs, or embayments. Thus, many of these types of systems are likely to experience difficulties in identifying the first-order region due to variable currents and wave energy. This is particularly true for HF radar systems operating in view of future offshore wind energy installations, where the rotating blades of the turbines have the potential to cause strong reflections that could result in variable noise conditions within the observed spectral estimates that serve as the basis for HF radar–based remote sensing of surface currents, waves, and winds. Thus, use of this type of updated FOL methodology will become increasingly important in the near future to obtain accurate environmental data that increase both marine domain awareness and coastal ocean research objectives.

*Acknowledgments.* This analysis was supported by internal funds from the Woods Hole Oceanographic Institution. The author thanks M. Kosro, H. Seim, M. Muglia, and S. Haines for providing portions of the HF data that were used in this analysis, which are available upon request (akirincich@whoi.edu) as well as archived in the WHOI Data Library (http://dla.whoi.edu).

## REFERENCES

Al-Lashi, R., S. Gunn, H. Czerski, R. S. Al-Lashi, S. R. Gunn, and H. Czerski, 2016: Automated processing of oceanic bubble images for measuring bubble size distributions underneath breaking waves. *J. Atmos. Oceanic Technol.*, **33**, 1701–1714, doi:10.1175/JTECH-D-15-0222.1.

Barrick, D. E., 1972: First-order theory and analysis of MF/HF/VHF scatter from the sea. *IEEE Trans. Antennas Propag.*, **20**, 2–10, doi:10.1109/TAP.1972.1140123.

——, and B. L. Weber, 1977: On the nonlinear theory for gravity waves on the ocean's surface. Part II: Interpretation and application. *J. Phys. Oceanogr.*, **7**, 11–21, doi:10.1175/1520-0485(1977)007<0011:OTNTFG>2.0.CO;2.

Beucher, S., 1993: The watershed transformation applied to image segmentation. *Proceedings of the 10th Pfefferkorn Conference on Signal Image Processing in Microscopy and Microanalysis*, P. W. Hawkes, Ed., Scanning Microscopy International, 299–314.

Cook, T., L. Hazard, M. Otero, and B. Zelenke, Eds., 2008: Deployment and maintenance of a high-frequency radar for ocean surface current mapping: Best practices. Southern California Coastal Ocean Observing Tech. Rep., 39 pp.

COS, 2013: SeaSonde Radial Suite release 7. CODAR Ocean Systems.

Crombie, D., 1955: Doppler spectrum of sea echo at 13.56 Mc./s. *Nature*, **175**, 681–682, doi:10.1038/175681a0.

de Paolo, T., E. Terrill, and A. Kirincich, 2015: Improving SeaSonde radial velocity accuracy and variance using radial metrics. *Proc. OCEANS 2015—Genova*, Genoa, Italy, IEEE, 9 pp., doi:10.1109/OCEANS-Genova.2015.7271360.

Gonzalez, R. C., and R. E. Woods, 2008: *Digital Image Processing*. Prentice Hall, 954 pp.

Graber, H. C., B. K. Haus, R. D. Chapman, and L. K. Shay, 1997: HF radar comparisons with moored estimates of current speed and direction: Expected differences and implications. *J. Geophys. Res.*, **102**, 18 749–18 766, doi:10.1029/97JC01190.

Halle, C., 2008: HF radar processing using ''nearest-neighbor'' statistics. University of California, Davis, Bodega Marine Laboratory Tech. Rep. 26 pp.

Kirincich, A., 2016a: ImageFOL developer package. Woods Hole Oceanographic Institution. [Available online at https://github.com/akirincich/imageFOLs.git.]

——, 2016b: Remote sensing of the surface wind field over the coast ocean via direct calibration of HF radar backscatter power. *J. Atmos. Oceanic Technol.*, **33**, 1377–1392, doi:10.1175/JTECH-D-15-0242.1.

——, 2016c: The occurrence, drivers, and implications of submesoscale eddies on the Martha's Vineyard inner shelf. *J. Phys. Oceanogr.*, **46**, 2645–2662, doi:10.1175/JPO-D-15-0191.1.

Kirincich, A. R., and S. J. Lentz, 2017: The importance of lateral variability on exchange across the inner shelf of Martha's Vineyard, MA. *J. Geophys. Res. Oceans*, **122**, 2360–2381, doi:10.1002/2016JC012491.

——, T. de Paolo, and E. Terrill, 2012: Improving HF radar estimates of surface currents using signal quality metrics, with application to the MVCO high-resolution radar system. *J. Atmos. Oceanic Technol.*, **29**, 1377–1390, doi:10.1175/JTECH-D-11-00160.1.

——, S. J. Lentz, J. T. Farrar, and N. K. Ganju, 2013: The spatial structure of tidal and mean circulation over the inner shelf south of Martha's Vineyard, Massachusetts. *J. Phys. Oceanogr.*, **43**, 1940–1958, doi:10.1175/JPO-D-13-020.1.

Laws, K., J. D. Paduan, and J. Vesecky, 2010: Estimation and assessment of errors related to antenna pattern distortion in CODAR SeaSonde high-frequency radar ocean current measurements. *J. Atmos. Oceanic Technol.*, **27**, 1029–1043, doi:10.1175/2009JTECHO658.1.

Lipa, B. J., B. Nyden, D. S. Ullman, and E. Terrill, 2006: SeaSonde radial velocities: Derivation and internal consistency. *IEEE J. Oceanic Eng.*, **31**, 850–861, doi:10.1109/JOE.2006.886104.

Mathworks, 2013: MATLAB and Image Processing Toolbox release 2013a. The MathWorks, Inc.

Meyer, F., 1994: Topographic distance and watershed lines. *Signal Process.*, **38**, 113–125, doi:10.1016/0165-1684(94)90060-4.

NDBC, 2009: Handbook of automated data quality control checks and procedures. NOAA/NDBC Tech. Doc. 09-02, 78 pp.

Paduan, J. D., and L. Washburn, 2013: High-frequency radar observations of ocean surface currents. *Annu. Rev. Mar. Sci.*, **5**, 115–136, doi:10.1146/annurev-marine-121211-172315.

——, R. Delgado, J. F. Vesecky, Y. Fernandez, J. Daida, and C. Teague, 1999: Mapping coastal winds with HF radar. *Proceedings of the IEEE Sixth Working Conference on Current Measurement*, S. P. Anderson et al., Eds., IEEE, 28–32, doi:10.1109/CCM.1999.755209.

Pham, D. L., C. Xu, and J. L. Princ, 2000: Current methods in medical image segmentation. *Annu. Rev. Biomed. Eng.*, **2**, 315–337, doi:10.1146/annurev.bioeng.2.1.315.

Schmidt, R. O., 1986: Multiple emitter location and signal parameter estimation. *IEEE Trans. Antenna Propag.*, **34**, 276–280, doi:10.1109/TAP.1986.1143830.

Shapiro, L., and G. Stockman, 2001: *Computer Vision*. Prentice Hall, 279–325.

Wilkin, J., 2006: The summertime heat budget and circulation of southeast New England shelf waters. *J. Phys. Oceanogr.*, **36**, 1997–2011, doi:10.1175/JPO2968.1.

Yang, X., H. Li, and X. Zhou, 2006: Nuclei segmentation using marker-controlled watershed, tracking using mean-shift, and Kalman filter in time-lapse microscopy. *IEEE Trans. Circuits Syst. I*, **53**, 2405–2414, doi:10.1109/TCSI.2006.884469.